Influence of the Heliospheric Current Sheet on the Evolution of Solar Wind Turbulence

Chen Shi, Marco Velli, Anna Tenerani, Victor Réville, Franco Rappazzo

The Astrophysical Journal, 928:93 (11pp), 2022 March 20 https://doi.org/10.3847/1538-4357/ac558b

Influence of the Heliospheric Current Sheet on the Evolution of Solar Wind Turbulence

Chen Shi (时辰)[1], Marco Velli[1], Anna Tenerani[2], Victor Réville[3], and Franco Rappazzo[1]
[1] Earth, Planetary, and Space Sciences, University of California, Los Angeles Los Angeles, CA 90095, USA; cshi1993@ucla.edu
[2] Department of Physics, The University of Texas at Austin, TX 78712, USA
[3] IRAP, Université Toulouse III—Paul Sabatier, CNRS, CNES, Toulouse, France
Received 2022 January 5; revised 2022 February 9; accepted 2022 February 14; published 2022 March 29

Abstract

The effects of the heliospheric current sheet (HCS) on the evolution of Alfvénic turbulence in the solar wind are studied using MHD simulations incorporating the expanding-box model. The simulations show that, near the HCS, the Alfvénicity of the turbulence decreases as manifested by lower normalized cross-helicity and larger excess of magnetic energy. The numerical results are supported by a superposed-epoch analysis using OMNI data, which shows that the normalized cross-helicity decreases inside the plasma sheet surrounding HCS, and the excess of magnetic energy is significantly enhanced at the center of HCS. Our simulation results indicate that the decrease of Alfvénicity around the HCS is due to the weakening of radial magnetic field and the effects of the transverse gradient in the background magnetic field. The magnetic energy excess in the turbulence may be a result of the loss of Alfvénic correlation between velocity and magnetic field and the faster decay of transverse kinetic energy with respect to magnetic energy in a spherically expanding solar wind.

Unified Astronomy Thesaurus concepts: Interplanetary turbulence (830); Magnetohydrodynamical simulations (1966); Solar wind (1534)

1. Introduction

Turbulence is a pervasive phenomenon in fluids and plasmas and has been observed to be a major feature of the solar wind. It is thought to be one of the main processes leading to solar wind heating (e.g., Kiyani et al. 2015) and contributing to its acceleration from the solar corona (e.g., Belcher 1971; Leer et al. 1982), while also affecting the acceleration and transport of energetic particles. Thus, understanding the origin and evolution of solar wind turbulence is crucial for fully understanding the heliosphere as a whole.

Coleman (1968), using Mariner 2 data, showed that the power spectra of fluctuations in the solar wind have power-law scaling relations, indicating a well-developed turbulence. Belcher & Davis (1971) found that these fluctuations are mainly outward-propagating Alfvén waves, with nearly incompressible plasma density and magnetic field. An important question is how the Alfvénic fluctuation, or Alfvénic turbulence, evolves radially. In the 1970s, Wentzel–Kramers–Brillouin (WKB) (e.g., Alazraki & Couturier 1971; Belcher 1971; Hollweg 1974) theory of the radial evolution of the Alfvén wave amplitude was developed. Following these early works, non-WKB (e.g., Heinemann & Olbert 1980; Barkhudarov 1991; Velli 1993) theory shows that linear coupling between the outward- and inward-propagating Alfvén waves leads to frequency-dependent reflection of the waves. Magnetohydrodynamic (MHD) models were developed to account for the evolution of the turbulence spectra and other parameters such as the wave energy densities (e.g., Tu et al. 1984; Zhou & Matthaeus 1990; Zank et al. 1996).

Elsässer variables $\boldsymbol{z}^{\pm}=\boldsymbol{u}\pm\boldsymbol{b}$, where $\boldsymbol{u}$ and $\boldsymbol{b}$ are velocity and magnetic field expressed in Alfvén speed, i.e., $\boldsymbol{b}=\hat{\boldsymbol{b}}/\sqrt{4\pi\rho}$ with $\hat{\boldsymbol{b}}$ and ρ being the magnetic field and plasma density, are convenient in describing the Alfvénic fluctuations, as they represent the inward- and outward-propagating Alfvén waves, respectively. Two quantities have been used as important diagnostics of the Alfvénic turbulence, namely the normalized cross-helicity (σ_c), defined as

$$\sigma_c=\frac{|\boldsymbol{z}^-|^2-|\boldsymbol{z}^+|^2}{|\boldsymbol{z}^-|^2+|\boldsymbol{z}^+|^2}, \tag{1}$$

and the normalized residual energy (σ_r), defined as

$$\sigma_r=\frac{|\boldsymbol{u}|^2-|\boldsymbol{b}|^2}{|\boldsymbol{u}|^2+|\boldsymbol{b}|^2}. \tag{2}$$

Here, σ_c measures the relative amount of outward and inward wave energies and σ_r measures the relative amount of kinetic and magnetic energies. A large number of works were conducted with regard to the radial evolution of these two quantities in the solar wind (e.g., Roberts et al. 1987; Bavassano et al. 1998; Bruno et al. 2007; Chen et al. 2020; Shi et al. 2021), but two outstanding problems remain unresolved. First, the normalized cross-helicity decreases with radial distance to the Sun, and second, a prevailing negative value of residual energy is observed. It is known that, in a homogeneous medium with a uniform background magnetic field, the Alfvénic turbulence evolves toward a status in which only one wave population survives, i.e., $\sigma_c=\pm1$. This is the so-called "dynamic alignment" (Dobrowolny et al. 1980). In contrast to the theory, in the solar wind, the dominance of the outward Alfvén wave is gradually weakened during the radial propagation, as manifested by the decrease of $|\sigma_c|$. Besides, in a purely Alfvénic system, the kinetic and magnetic energies should be exactly equipartitioned, i.e., $\sigma_r=0$, while in the solar wind, a magnetic energy excess is typically observed even at distances very close to the Sun, below 30 solar radii (Chen et al. 2020; McManus et al. 2020; Shi et al. 2021).

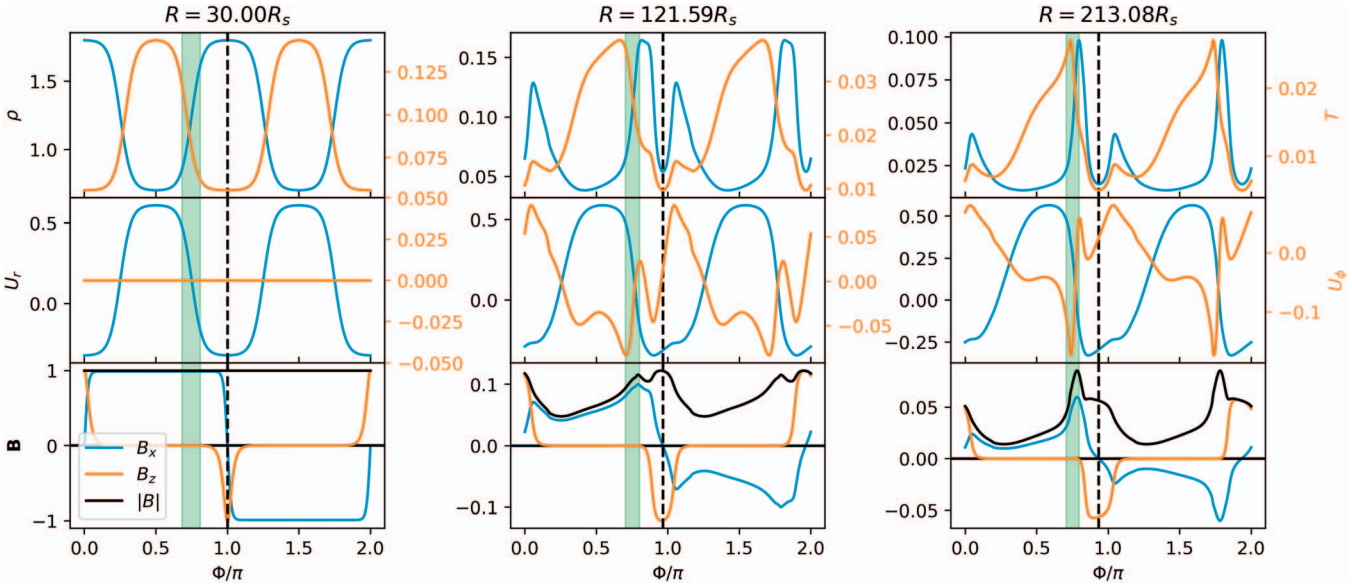

Figure 1. Evolution of the longitudinal profiles of background fields from a 1D run without any waves. Left column is the initial status at 30R_s, middle column is at 121.59R_s, and right column is around 1 au. Top row: density (blue) and temperature (orange). Middle row: radial speed (blue) in the expanding-box frame and longitudinal speed (orange). Bottom row: radial component (blue), out-of-plane component (orange), and magnitude (black) of the magnetic field. The quantities are normalized (see the text). The green shade shows the compression region, and the vertical dashed line marks the polarity reversal of the magnetic field.

One possible mechanism that resolves these paradoxes is the large-scale velocity shear in the solar wind. Coleman (1968) proposed that the differential streaming generates Alfvén waves at long wavelengths. These newly generated waves do not have a preferential propagating direction, and thus the initial dominance of the outward wave gradually declines. This shear-driven decrease of cross-helicity was confirmed by numerical simulations (Roberts et al. 1992; Shi et al. 2020). Velocity shear is widely adopted in turbulence models as a source for the wave energies, and is able to reproduce the observed decrease of σ_c in the models. On the contrary, there has been no satisfactory solar wind turbulence model that leads to negative residual energy so far. For example, in the model by Zank et al. (2017), the source term for the residual energy is attributed to the stream shear, but whether this term causes growth or decay of the residual energy is arbitrary. The heliospheric current sheet (HCS) is a good candidate that may influence the evolution of Alfvénic turbulence. It is shown by both simulations and in situ observations that, in the proximity of the HCS, the Alfvénicity of the turbulence decreases in general (e.g., Goldstein & Roberts 1999; Chen et al. 2021). However, how the HCS modifies the dynamic evolution of σ_c and σ_r in the spherically expanding solar wind is still unclear.

In this study, we carry out two-dimensional MHD simulations using the expanding-box model (EBM). Large-scale solar wind structures, including the fast–slow stream interaction regions (SIRs) and the HCS, are constructed and evolve self-consistently in the simulations. We investigate how properties of the Alfvénic turbulence evolve radially and how SIRs and HCS modify its evolution. A superposed-epoch analysis of HCS crossings at 1 au is carried out using the OMNI data set, and the turbulence properties near the HCS are examined. The paper is organized as follows. In Section 2, we present the setup of the MHD simulations and the numerical results. In Section 3, we present the superposed-epoch analysis of the HCS crossings observed at 1 au. We then discuss our results in Section 4 and conclude in Section 5.

2. Expanding-box Model Simulation

2.1. Numerical Method and 1D Test Run

The code we use for simulations is a 2D pseudo-spectral MHD code used by Shi et al. (2020) to study the interaction between SIRs and turbulence. The EBM module is implemented so that the radial expansion effect of the solar wind is taken into account (Grappin et al. 1993; Grappin & Velli 1996). The expansion effect is not negligible in the solar wind, because it induces inhomogeneity of the background streams, which leads to the reflection of the Alfvén waves (e.g., Heinemann & Olbert 1980) and anisotropic evolution of velocity and magnetic fields in the radial and transverse directions (e.g., Dong et al. 2014). The EBM has also been employed to reproduce the "magnetic switchbacks" observed in the young solar wind (Squire et al. 2020). In our code, a finite spiral angle of magnetic field and stream interface is allowed so that compression and rarefaction regions are constructed. A detailed description of the numerical method can be found in Shi et al. (2020).

We carried out four simulations with two free parameters, namely whether a nonzero spiral angle is set and whether the expansion effect is included. Here, we mainly present results from the run with both a nonzero spiral angle and the expansion effect, i.e., the most realistic run. The parameters for the initial setup are chosen according to solar wind observations as described below. The simulation starts from $R_0 = 30R_s$ and ends at $R = 270.9R_s$, where R_s is the solar radius. The initial spiral angle is $\alpha = 8.^\circ1$ so that the angle becomes 45° at 1 au. The size of the simulation domain is $L_{x'} \times L_{y'} = 10R_s \times 2\pi R_0$, where $x' - y'$ is the corotating coordinate system, i.e., x' is parallel to the background magnetic field and y' is the quasi-longitudinal direction (Shi et al. 2020). $L_{y'} = 2\pi R_0$ means that the domain is a full circle in the ecliptic plane. The initial background fields as functions of the quasi-longitudinal direction y' are plotted in the left column of Figure 1 with normalized units. The quantities for normalization are: $\bar{n} = 200$ cm^{-3}, $\bar{B} = 250$ nT, $L = R_s$,

$\bar{V} = \bar{B}/\sqrt{4\pi m_p \bar{n}} = 386$ km s^{-1}, and $\bar{P} = \bar{B}^2/4\pi = 49.7$ nT. The wind consists of two fast streams and two slow streams. The transition between fast and slow streams is of the form $\tanh(y'/a_{sh})$, where $a_{sh} = 0.075\pi R_0$. The velocity of the streams is purely radial, with the speed ranging from 340 to 700 km s^{-1}. We note that, in Figure 1, the velocity is in the reference frame of the expanding box, which moves radially with the average speed of the plasma inside the simulation domain $U_0 = 464$ km s^{-1}. The density is 360 cm^{-3} for the slow streams and 140 cm^{-3} for the fast streams. Two Harris current sheets with thickness $a_{cs} = 0.025\pi R_0$ are embedded in the center of the slow streams. The current sheets are force-free, as the in situ measurement of the HCS usually shows (Smith 2001), and a finite z-component is used to make sure that $|\boldsymbol{B}|$ is constant and the magnetic field strength is uniformly 250 nT. The pressure is uniform and equals 5 nPa, i.e., the plasma beta is $\beta = 8\pi p/B^2 \approx 0.2$, so that the temperatures of the fast and slow streams are 2.6 MK and 1.0 MK, respectively. The adiabatic index is set to be $3/2$ instead of $5/3$, since the solar wind observations show that the cooling rate of the solar wind is slower than a $5/3$ adiabatic cooling (e.g., Hellinger et al. 2011).

In Figure 1, we show the evolution of the background fields from a 1D run with grid points on the y'-axis, i.e., the quasi-longitude direction. The top row shows density (blue) and temperature (orange); the middle row shows the radial component (blue) and transverse component (orange) of the velocity; and the bottom panel shows the radial component (blue), out-of-plane component (orange), and the magnitude (black) of the magnetic field. From left to right, the columns are the profiles of the background fields at three locations as labeled on the top. In each column, the green shade shows one of the two compression regions and the vertical dashed line marks one of the polarity reversal points of the radial magnetic field. We can see that, as the simulation proceeds, a compression region with enhanced density, temperature, and magnetic field strength forms between the trailing fast stream and leading slow stream. A divergent transverse flow due to the deflection of the streams is also observed in the compression region. In the rarefaction region, i.e., the trailing edge of the fast slow, the density, temperature, and magnetic field strength decrease. But we note that, near the current sheet, a dip is seen in density and temperature but the magnetic field strength shows a peak. This is a result of the differential decay rates of B_z and B_x induced by the expansion of the solar wind. As $B_z \propto 1/R$ decays slower than $B_x \propto 1/R^2$, an initial force-free current sheet cannot maintain a uniform magnetic pressure once the expansion starts and a local peak of magnetic pressure forms at the polarity reversal point. The large magnetic pressure will then push the plasma away from the current sheet, resulting in a local dip in density and temperature and also a divergent transverse flow.

2.2. Results of the 2D Runs with Waves

Based on the 1D run, 2D simulations are conducted. At initialization, circularly polarized Alfvénic wave bands comprising 16 modes are added on top of the background streams with wave vectors parallel to $\hat{e}_{x'}$ and correlated $\boldsymbol{u}$ & $\boldsymbol{b}$ fluctuations in the y' & z directions (see Shi et al. (2020) for more details). The energy spectrum of the initial waves obeys $E(k_{x'}) \propto k_{x'}^{-1}$, with $k_{x',m} = m/L_{x'}$, where $m = 1, 2, \cdots 16$, i.e., the longest and shortest wavelengths are $10R_s$ (wave period $T \approx \lambda/U_0 = 4$ hr) and $0.625R_s$ (wave period $T \approx \lambda/U_0 = 15$ minutes), respectively. Both outward and inward waves are added, with the amplitude of the inward waves being $1/5$th of the amplitude of the outward waves. The amplitude of the first mode of the outward waves is $0.2B_0 = 50$ nT. To avoid sharp jumps of perturbation fields across the current sheets, we modulate the wave amplitudes by a hyperbolic tangent function, similar to the x'-component of the background magnetic field, such that the wave amplitudes are exactly zero at the center of the current sheets. Note that this requires nonzero wave components along x' inside the current sheets, to ensure $\nabla \cdot \boldsymbol{B} = 0$. The number of grid points is $n_{x'} \times n_{y'} = 2048 \times 8192$ (we note that the simulation domain size is $10R_s \times 60\pi R_s$) so that the smallest wavelength that is resolved is $\lambda = 2\Delta x' \approx 0.01R_s$, corresponding to a wave period $T \approx \lambda/U_0 \approx 15$ s, which is approximately two magnitudes larger than the ion gyroscale and ion inertial scale. But we note that, in the MHD simulations, there are no intrinsic gyroscales and inertial scales—or in other words, these kinetic scale lengths are zero in MHD.

We process the simulation data using the same method as described in Shi et al. (2020). At each time—or equivalently, each radial distance to the Sun—we first calculate the x'-averaged fields, i.e., the background fields. Then we remove the background fields to get the wave fields. We only analyze wave components that are perpendicular to the $x-y$ plane background magnetic field $\boldsymbol{B}_0 = B_0(y')\hat{e}_{x'}$. We note here that, in the $x-y$ plane, the background magnetic field is always aligned with $\hat{e}_{x'}$, as the x'-axis rotates away from the radial direction as the solar wind expands (Shi et al. 2020). The perturbed Elsässer variables are defined by

$$\boldsymbol{z}_{\rm out} = \boldsymbol{u}_1 - {\rm sign}(B_0)\frac{\boldsymbol{b}_1}{\sqrt{\rho}},\ \boldsymbol{z}_{\rm in} = \boldsymbol{u}_1 + {\rm sign}(B_0)\frac{\boldsymbol{b}_1}{\sqrt{\rho}}. \quad (3)$$

We then apply a Fourier transform along x' to $\boldsymbol{u}_1$, $\boldsymbol{b}_1/\sqrt{\rho}$, $\boldsymbol{z}_{\rm out}$, and $\boldsymbol{z}_{\rm in}$. As there are 2048 grid points along x', 1024 wave modes are resolved with wavenumbers $k_{x'} = (1, 2, \cdots 1024)/L_{x'}$, i.e., mode m corresponds to $k_{x'} = m/L_{x'}$. We divide all the wave modes into 10 wavenumber bands, which are logarithmically spaced, i.e., band i contains modes $[2^{i-1}, 2^i)$, or wavelengths between $L_{x'}/2^{i-1}$ and $L_{x'}/2^i$. We then calculate $\sigma_c(y')$ and $\sigma_r(y')$ for each wavenumber band and also for integration of all wave modes.

In Figure 2, we present the $y' - R(t)$ profiles color-coded with σ_c (top row) and σ_r (bottom row) for all wave modes (left column) and for band 03 (right column), which corresponds to a wavelength of $\lambda \in [2.5R_s, 1.25R_s)$, or roughly to a wave period of $T \in [38, 75)$ minutes. The figure is produced by piling up the y' profiles of $\sigma_{c,r}$ at different moments—or equivalently, different radial locations $R(t)$. In the top left panel, we use dashed lines to mark the boundaries of fast streams, defined as $y'(t)$ at which the background radial speed equals 650 km s^{-1}, and we use dashed black lines to mark the boundaries of slow streams, defined as $y'(t)$, at which the background radial speed equals 400 km s^{-1}. The two current sheets are located in the center of the slow streams, around $y' = 0.5L_{y'}$ and $y' = L_{y'}$. We first inspect the left column of Figure 2, which shows σ_c and σ_r calculated using wave energies integrated over all wavenumbers. As already discussed by Shi et al. (2020), in regions with nearly uniform background fields, i.e., inside fast

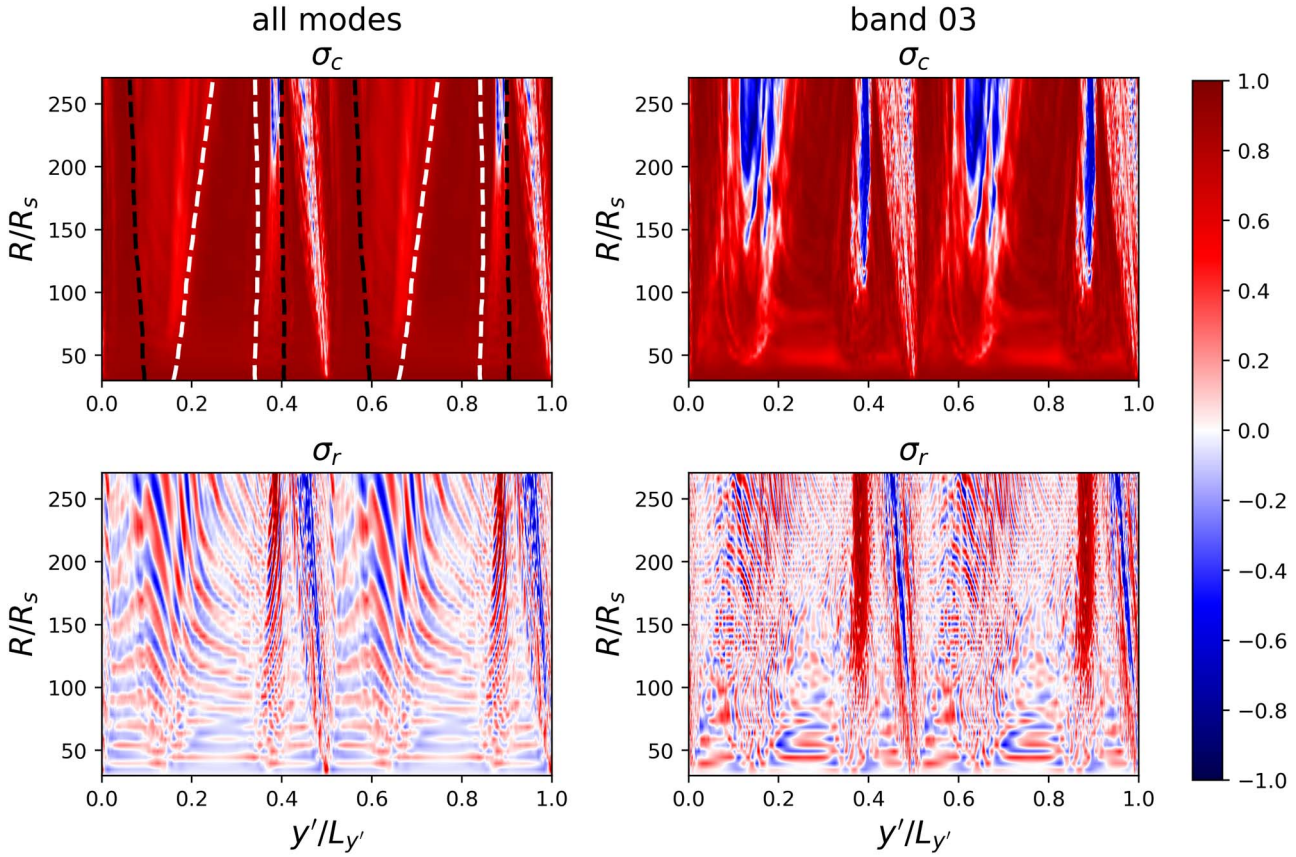

Figure 2. $y' - R(t)$ profiles color-coded with the normalized cross-helicity σ_c (top row) and the normalized residual energy σ_r (bottom row). Left column is the result using wave energies integrated over all modes, and right column is the result for wave modes [4, 8), or wavelength $\lambda \in [2.5R_s, 1.25R_s)$, corresponding roughly to wave period $T \in [38, 75)$ minutes. In the top left panel, the dashed white lines mark the boundaries of fast streams, defined as $y'(t)$, at which the background radial speed equals 650 km s^{-1}, and the dashed black lines mark the boundaries of slow streams, defined as $y'(t)$, at which the background radial speed equals 400 km s^{-1}.

streams and inside slow streams far from the current sheets, σ_c remains almost constant throughout the evolution, indicating that the Alfvénicity remains high in these regions. In the velocity-shear regions (regions between the black and white lines), σ_c declines with radial distance. In particular, in the compression region (around $y' = (0.35 - 0.4)L_{y'}$ and $y' = (0.85 - 0.9)L_{y'}$), σ_c drops below 0 beyond 200R$_s$. Shi et al. (2020) showed that, in shear regions, the damping of the outward Alfvén wave is significantly faster than the inward Alfvén wave, leading to the decrease in σ_c. Except for near the current sheets, which will be discussed in detail later, σ_r oscillates around zero in all regions, indicating that the Alfvénicity of the waves is well-conserved for the long-wavelength modes (we note that the integrated wave energies are dominated by the modes of largest scales). The oscillation in σ_r is caused by periodic correlation and decorrelation between the outward and inward waves. From the left column of Figure 2, we also see that the evolution of Alfvén waves is significantly modified by the current sheets. In the neighborhood of the current sheets, σ_c decreases quite fast and σ_r evolves toward negative values. In the left panel of Figure 3, we plot the radial evolution of σ_c and σ_r in a band of width 2a$_{cs}$ around the current sheet initially located at $y' = 0.5L_{y'}$. Here, σ_c starts from a high value, i.e., 0.92, determined by the initial condition, drops to around 0.2 within $100R_s$, and then remains stable. The value of σ_r starts at exactly zero, rises slightly at the beginning due to the increase of kinetic energy caused by the magnetic pressure gradient at the current sheet as discussed in Section 2.1, and then starts to drop continuously, reaching a value of -0.3 at 1 au. For comparison, we plot the time evolution of σ_c and σ_r from the run without expansion in the right panel of Figure 3. Evolution of σ_c does not show much difference between the two runs, while σ_r remains around zero in the run without expansion, indicating that the expansion effect is important to the decrease of σ_r around the current sheet, which will be discussed in more detail in Section 4.

In the right column of Figure 2, we show the $y' - R(t)$ profiles of σ_c and σ_r for wave band 03. Compared with the left column, the drop of σ_c in velocity-shear regions is much more significant and the σ_c-drop regions around the current sheets are wider. For σ_r, the most prominent feature is that, inside the compression regions, σ_r evolves toward $+1$, i.e., kinetic energy becomes dominant in these regions, indicating that the large-scale velocity shear and compression facilitate the transfer of kinetic energy toward small scales.

In Figure 4, we show the x' spectra, i.e., the parallel spectra, of various fields calculated at the moment $R(t) = 217.9R_s$. From left to right, columns are spectra averaged in y' bands of width 2a$_{cs}$ inside the fast stream, current sheet, and compression region, respectively. The top row shows the spectra of outward (blue) and inward (orange) Elsässer variables. The middle row shows the spectra of kinetic (blue) and magnetic (orange) perturbations. We multiply these spectra by $k_{x'}^2$, as the "critical balance" model (Goldreich & Sridhar 1995) predicts a parallel spectrum $E \propto k_{\parallel}^{-2}$. We can see from Figure 4 that, in general, these spectra are steeper than the prediction of the critical

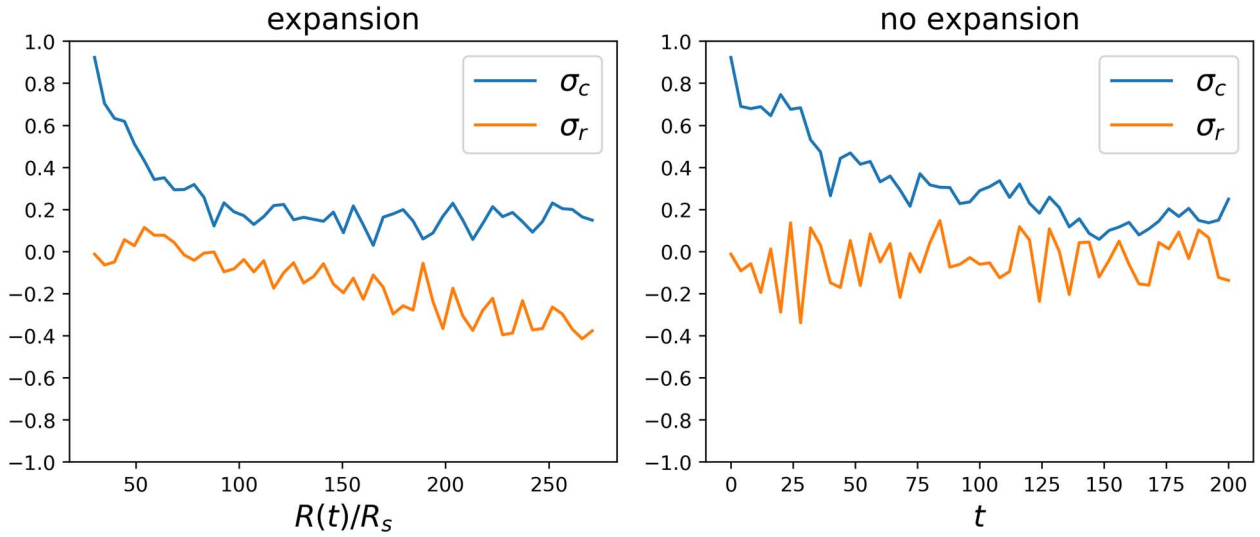

Figure 3. Left: radial evolution of σ_c (blue) and σ_r (orange) in a longitude band with thickness $2a_{cs}$ around the current sheet in the run with expansion (Figure 2). Right: similar to left panel, time evolution of σ_c (blue) and σ_r (orange) near the current sheet in the run without expansion.

balance model except for inside the fast stream. This is because the shears in magnetic field and velocity turn the wavevector from quasi-parallel to quasi-perpendicular and gradually enlarge the perpendicular wavenumber, which speeds up the dissipation of the wave energies (Shi et al. 2020). The bottom row shows the spectra of σ_c and σ_r calculated from the spectra shown in the top and middle rows. Inside the fast stream, σ_c is close to unity and σ_r is close to zero for most modes, except for close to the numerical dissipation range, meaning that the waves maintain a high Alfvénicity over a large span of wavenumbers. Around the current sheet, σ_c decreases to nearly zero for all wavenumbers. The value of σ_r is negative for most of the wavenumbers, except for an intermediate range ($1 < k_{x'}R_s < 3$) where it is around zero. In the compression region, σ_c is overall smaller than the initial condition 0.92, but the curve of σ_c shows a decrease with $k_{x'}$ at small wavenumbers and rises again. The value of σ_r is around zero for small wavenumbers, and it shows a significant increase with $k_{x'}$, reaching its maximum value at the same $k_{x'}$ where σ_c reaches its local minimum. This indicates that, in the compression region, the large-scale stream structure generates small-scale fluctuations that are dominated by kinetic energy, as observed in previous simulations (e.g., Roberts et al. 1992). The newly generated fluctuations weaken the dominance of the outward Alfvén waves, consistent with the scenario proposed by Coleman (1968). We note that, for large wavenumbers ($k_{x'}R_s \gtrsim 5$) the spectra are significantly modulated by the explicit numerical filter applied to the simulation, thus spectral breaks can be seen at large wavenumbers.

We do not present the perpendicular power spectra, for the following reasons. First, as the simulation coordinate system is non-Cartesian, there is no axis perpendicular to $\boldsymbol{B}_0$. The y'-axis is perpendicular to $\boldsymbol{B}_0$ initially, but the angle between y' and $\boldsymbol{B}_0$ gradually increases (Shi et al. 2020). Second, because of the elongated simulation domain along y', and also due to the spherical expansion, the resolution in y' is much lower than that in x'. Besides, as we would like to focus on certain longitudinal regions, e.g., around the HCS, instead of the whole y' range, the number of data points is limited. Because of the above reasons, it is difficult to produce physically meaningful perpendicular spectra.

In Figure 5, we plot the y' profiles of the normalized density fluctuation $\delta\rho/\rho$ (blue) and the square of the Mach number $(\delta u/C_s)^2$ (orange) in the simulation at moment $R(t) = 217.91R_s$. Here, $\delta\rho$ and δu are the root-mean-squares of density and velocity calculated long x'. C_s is the speed of sound. Yellow and green shades mark the fast and slow streams, respectively. The vertical dashed lines are the locations of the current sheets. The normalized density fluctuation is overall small, mostly below 0.2, similar to the solar wind observation (e.g., Shi et al. 2021). In the compression region and near the current sheet, e.g., from $\Phi = 0.7 - 1.1$, $\delta\rho/\rho$ is highly correlated with $(\delta u/C_s)^2$, implying a large compressive component in the velocity fluctuations in these regions.

3. Superposed-epoch Analysis of HCS at 1 au

Although works have been carried out with regard to turbulence properties around SIRs (e.g., Borovsky & Denton 2010), literature on how HCS affects the solar wind turbulence is still incomplete. To validate our simulation results, we carry out a superposed-epoch analysis of HCS crossings at 1 au and study how the properties of turbulence change near HCS.

3.1. Selection and Structure of HCS

For the current study, we use the OMNI data set, which contains magnetic field and plasma data from multiple spacecraft, including ACE and WIND (King & Papitashvili 2005). The time resolution of the data is 1 minute, sufficient for the study of MHD turbulence. We analyze data during two 4 yr periods: 2000–2003, which is around the solar maximum of solar cycle 23, and 2007–2010, which is around the solar minimum between solar cycles 23 and 24, as shown by the shaded regions in Figure 6, which plots monthly sunspot numbers.

The procedure to select HCS crossings can be stated as follows. We first calculate the one-day average of $B_{x,\mathrm{GSE}}$, which is equivalent to the opposite of the radial component of the solar wind magnetic field. Next, we find days when its polarity changes, and we require that the polarities before and after each polarity-reversal day are maintained for at least 4

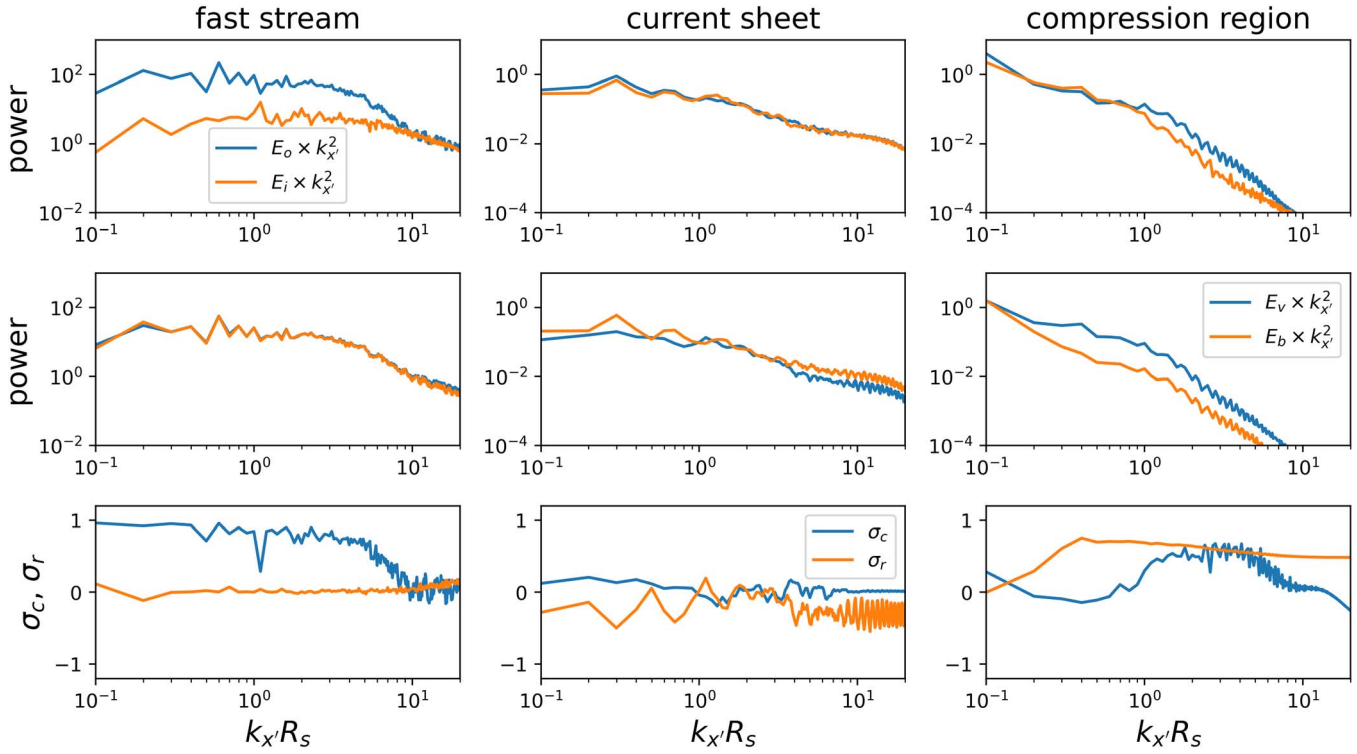

Figure 4. The x' spectra of various fields at $R(t) = 217.9R_s$ inside the fast stream (left column), the current sheet (middle column), and the compression region (right column). The spectra are averaged in a y' band of width $2a_{cs}$ inside each region. Top row: spectra of the outward (blue) and inward (orange) Alfvén waves (Elsässer variables). Middle row: spectra of the kinetic (blue) and magnetic (orange) perturbations. Bottom row: spectra of σ_c (blue) and σ_r (orange) calculated from the spectra in top and middle rows.

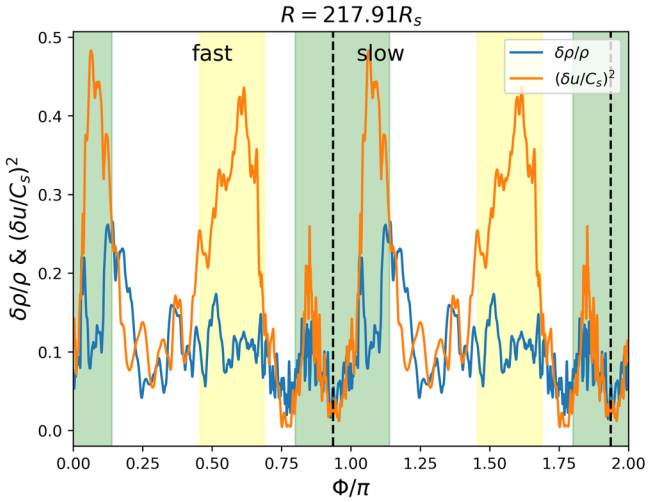

Figure 5. Longitude profiles of the normalized density fluctuation $\delta\rho/\rho$ (blue) and the square of the Mach number $(\delta u/C_s)^2$ (orange) in the simulation at moment $R(t) = 217.91R_s$. $\delta\rho$ and δu are the root-mean-squares of density and velocity calculated along x'. C_s is the speed of sound. Yellow and green shades mark the fast and slow streams, respectively. The vertical dashed lines are the locations of the current sheets.

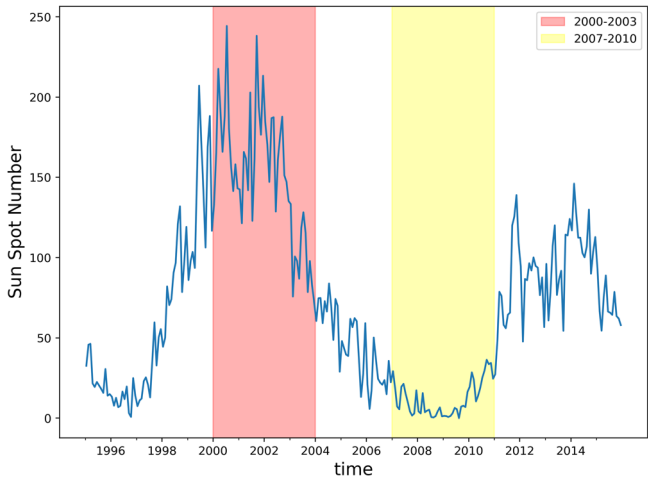

Figure 6. Monthly sunspot numbers from 1995 to 2015. The two shaded regions mark the two time periods used for OMNI data analysis and correspond to the solar maximum (2000–2003) and solar minimum (2007–2010), respectively.

days. Then we inspect the 1 minute data to determine the exact polarity reversal times. We identify 48 events for the solar maximum and 45 events for the solar minimum. A list of the HCS crossings is shown in Table 1.

A superposed-epoch analysis of the HCS structure is shown in Figure 7. From top to bottom, the rows show the GSE B_x, GSE B_y, V_r, GSE V_y, proton density, and proton temperature, respectively. The left column is the solar maximum and right column is the solar minimum. In each panel, gray curves are individual events and the blue curve is the median value of all events. In the top two rows, we also plot medians of the magnetic field strength in black curves. We have reversed the time series of certain events such that B_x is always changing from negative to positive. The timescale for HCS crossings is on average 1–2 hr, and the HCS is embedded in much thicker (1–2 days) plasma sheets with enhanced proton density and lower proton temperature. The magnetic field strength is quite constant across the HCS, implying a force-free structure. By comparing the left and right columns of Figure 7, we see that

Table 1
List of HCS Crossings Identified Using OMNI Data

#	Year	Month	Day	Hour	Minute
01	2000	01	10	00	30
02	2000	02	05	17	50
03	2000	07	31	19	40
04	2000	08	27	17	33
05	2000	09	24	15	50
06	2000	10	14	18	04
07	2000	11	23	19	33
08	2000	12	16	21	03
09	2000	12	22	21	23
10	2001	01	10	21	03
11	2001	02	14	07	17
12	2001	03	12	14	55
13	2001	04	22	00	23
14	2001	05	06	10	40
15	2001	05	17	21	32
16	2001	06	29	06	21
17	2001	07	10	16	30
18	2001	07	24	15	05
19	2001	11	16	11	28
20	2002	02	04	21	21
21	2002	03	03	22	49
22	2002	05	06	09	55
23	2002	06	02	02	40
24	2002	06	16	06	08
25	2002	06	25	16	37
26	2002	09	03	06	46
27	2002	09	27	05	29
28	2002	10	23	17	02
29	2002	11	10	02	57
30	2002	12	06	11	21
31	2002	12	19	07	41
32	2003	01	17	14	08
33	2003	02	12	22	54
34	2003	02	26	19	48
35	2003	03	11	17	18
36	2003	03	26	09	40
37	2003	04	08	02	34
38	2003	04	20	19	07
39	2003	05	04	16	00
40	2003	05	18	16	23
41	2003	06	26	12	30
42	2003	07	11	15	25
43	2003	07	26	12	01
44	2003	08	04	06	52
45	2003	09	01	06	13
46	2003	10	13	09	27
47	2003	12	05	01	26
48	2003	12	19	19	50
01	2007	01	08	02	01
02	2007	01	15	08	39
03	2007	02	04	01	44
04	2007	02	12	15	17
05	2007	03	03	08	18
06	2007	03	11	18	17
07	2007	03	31	23	21
08	2007	06	02	15	19
09	2007	06	08	01	24
10	2007	06	13	18	59
11	2007	08	05	16	02
12	2007	08	31	20	25
13	2007	09	09	23	45
14	2007	10	11	06	22
15	2007	11	20	09	33
16	2007	12	17	06	12

Table 1
(Continued)

#	Year	Month	Day	Hour	Minute
17	2008	01	12	13	06
18	2008	01	31	15	24
19	2008	02	07	17	25
20	2008	02	27	17	03
21	2008	03	08	08	01
22	2008	04	03	03	00
23	2008	04	22	15	28
24	2008	04	30	16	56
25	2008	06	25	16	14
26	2008	07	21	03	41
27	2008	07	30	10	50
28	2008	08	24	23	43
29	2008	11	07	03	51
30	2008	12	03	15	40
31	2008	12	11	00	09
32	2009	01	23	13	54
33	2009	02	03	00	59
34	2009	04	15	08	27
35	2009	05	13	19	36
36	2009	06	20	19	18
37	2009	07	13	13	23
38	2009	07	20	10	21
39	2010	01	31	02	21
40	2010	03	01	06	52
41	2010	03	14	23	10
42	2010	06	06	23	58
43	2010	08	20	10	01
44	2010	11	12	11	26
45	2010	12	23	16	26

the strength of magnetic field is larger during the solar maximum than the solar minimum. Another thing to notice is that there is a negative GSE V_y at the HCS, i.e., the plasma flow is rotating in the same direction with the solar rotation. The reason might be that HCS is usually embedded in slow solar wind ahead of the compression region and pushed along the longitudinal direction in accordance with solar rotation (Siscoe 1972; Eselevich & Filippov 1988).

3.2. Turbulence Properties near HCS

We then analyze turbulence properties near the HCS. We use a running time window of width 128 minutes. Any time window with a data gap ratio larger than 20% is not considered. Inside each time window, we first apply linear interpolation to velocity, magnetic field, and proton density, to fill the data gaps. Then we calculate Elsässer variables after determining the polarity of radial magnetic field by averaging B_x in the time window. Finally, we apply a Fourier transform to these fields. Following a method similar to the process applied to simulation data in the prior section, we divide the frequency into six bands such that band i contains wave modes $[2^{i-1}, 2^i)$, e.g., wave band 6 contains waves whose periods are between $128/2^5 = 4$ minutes and $128/2^6 = 2$ minutes. We calculate σ_c and σ_r for each wave band by integrating wave energies in each band. In addition, we fit the power spectra and get the spectral slopes for velocity, magnetic field, and the outward and inward Elsässer variables.

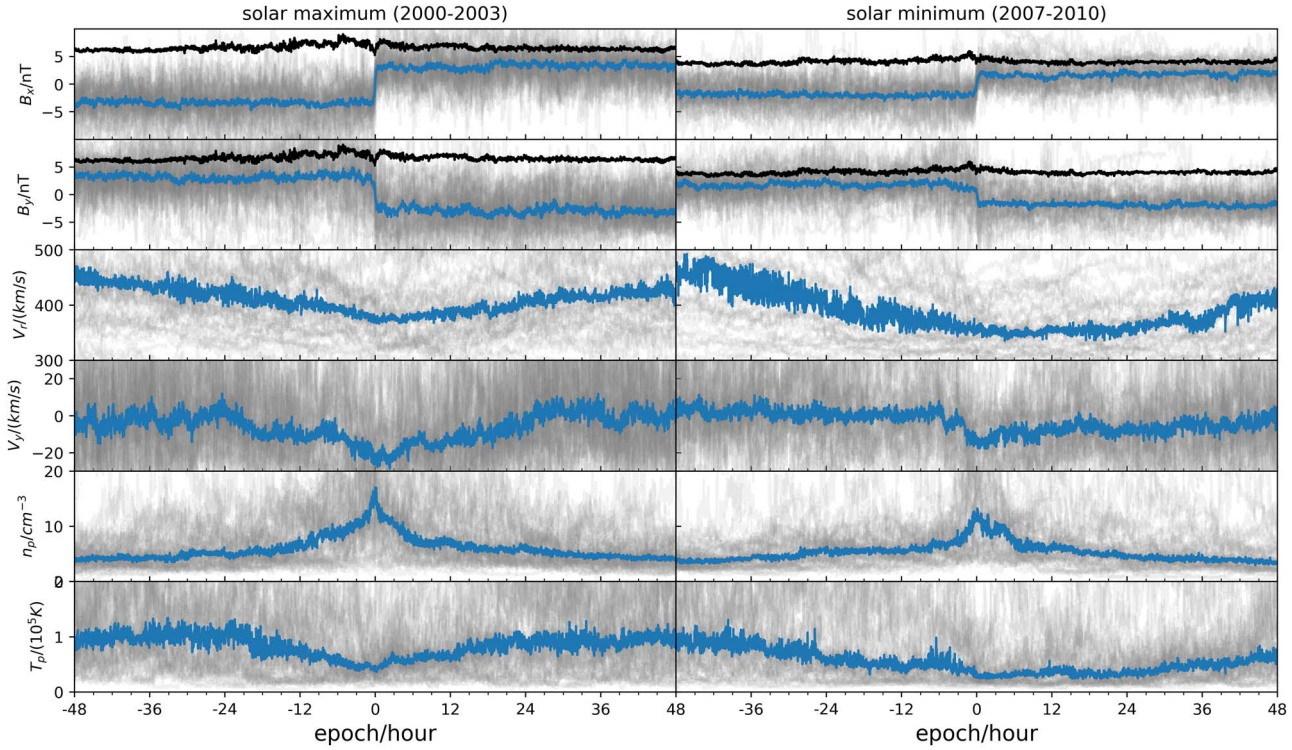

Figure 7. Superposed-epoch analysis of the HCS crossings. Epoch 0 is the moment of crossing. From top to bottom, the rows show B_x and B_y in GSE coordinates, V_r, GSE V_y, proton density, and proton temperature, respectively. Left column is solar maximum and right column is solar minimum. In each panel, the gray lines are individual events and the blue line is the median value. In the top two rows, the black curves are the medians of $|\boldsymbol{B}|$.

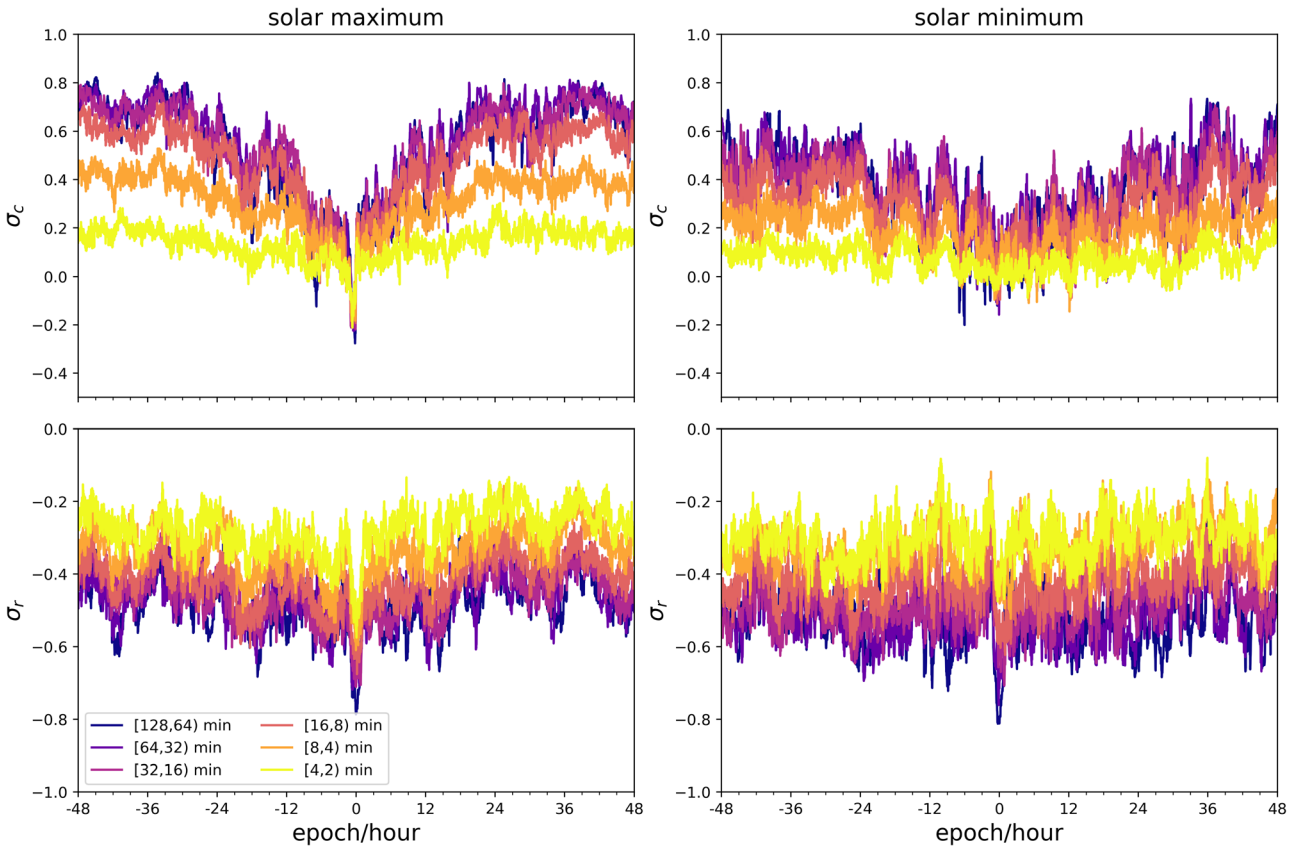

Figure 8. Superposed-epoch analysis of σ_c (top row) and σ_r (bottom row) near HCS. Left column is solar maximum and right column is solar minimum. In each panel, dark to light colors are wave bands 1–6, respectively, i.e., from low to high frequencies.

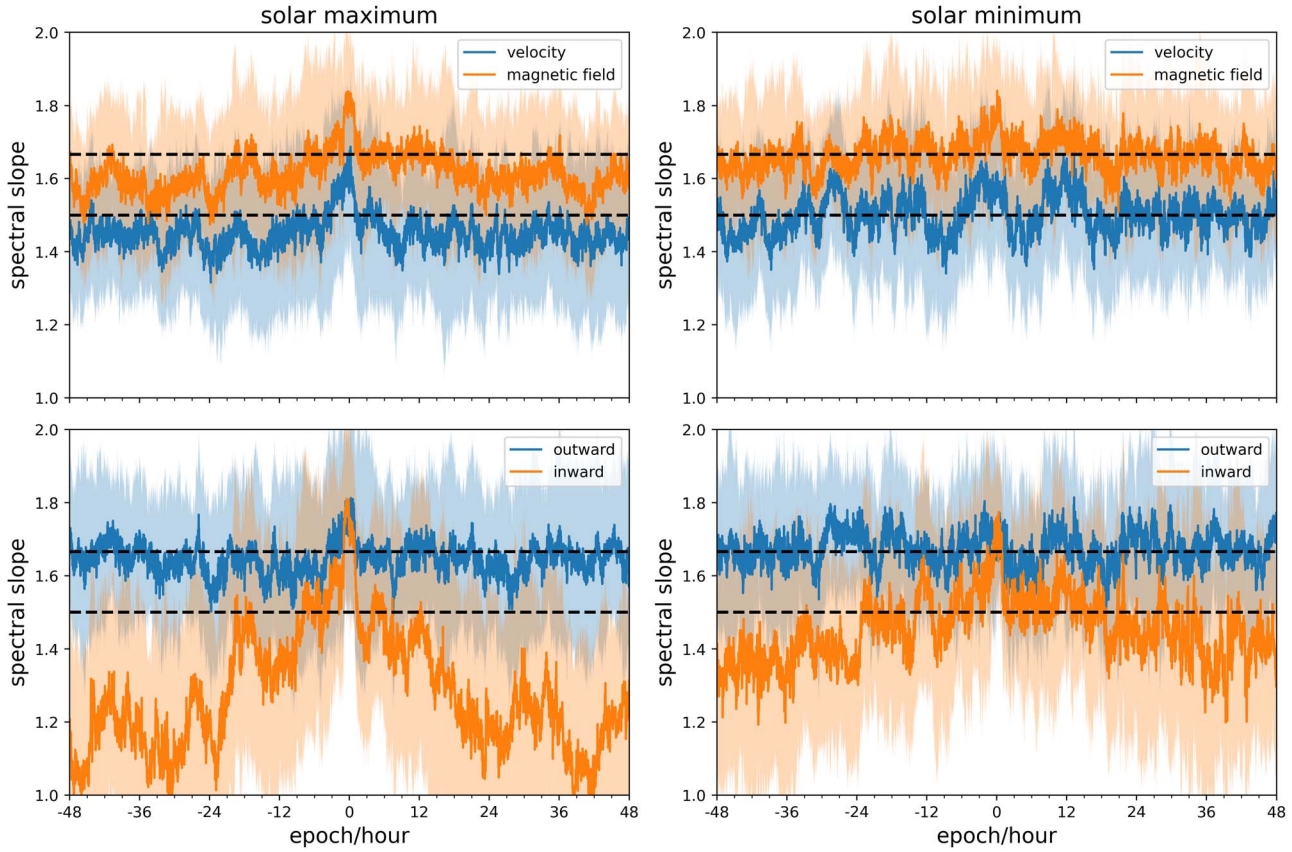

Figure 9. Superposed-epoch analysis of various spectral slopes near HCS. Top panels show slopes of velocity (blue) and magnetic field (orange), and bottom panels show slopes of outward (blue) and inward (orange) Elsässer variables. Left column is solar maximum and right column is solar minimum. In each panel, the two horizontal lines mark the values $3/2$ and $5/3$ for reference. The shaded bands show the standard deviations of different curves.

In Figure 8, we show superposed-epoch analysis of σ_c (top row) and σ_r (bottom row). The left column is the solar maximum and the right column is the solar minimum. Colors represent different wave bands such that dark to light colors are bands 1–6. We see that, in general, σ_c decreases with frequency while σ_r increases with frequency. The top left panel shows that, in a time window of ± 1 day, approximately the width of the plasma sheet, σ_c drops as we approach the center of HCS. In a narrow window of width comparable to the thickness of HCS, i.e., 1–2 hr, σ_c drops significantly because the outward and inward waves mix with each other. The bottom left panel of Figure 8 shows a slight decrease of σ_r inside the plasma sheet while a large drop of σ_r is observed near HCS. During the solar minimum (right column of Figure 8), the above results qualitatively hold, but both σ_c and σ_r are lower compared with the solar maximum.

In Figure 9, we show the superposed-epoch analysis of various spectral slopes. Again, the left and right columns are the solar maximum and solar minimum, respectively. In the top row, the blue and orange curves are the spectral slopes of the velocity and magnetic field. In the bottom row, the blue and orange curves are the spectral slopes of the outward and inward Elsässer variables. In each panel, the two horizontal dashed lines mark the values $5/3$ and $3/2$ for reference. Away from the HCS, velocity spectrum has a slope near $-3/2$ and magnetic field spectrum has a slope near $-5/3$ as typically observed in the solar wind (e.g., Chen et al. 2020; Shi et al. 2021). Near the center of HCS, both of the two spectra steepen, and the steepening is more pronounced during the solar maximum. The outward Elsässer variable has a spectral slope near $-5/3$ and shows a slight steepening near HCS during solar maximum while no obvious steepening is observed during solar minimum. The variation in spectral slope of the inward Elsässer variable is more dramatic compared with the other quantities. The $z_{\rm in}$ spectrum is quite flat far from the HCS, around -1 during solar maximum and -1.2 during solar minimum. We note that, in our simulation (top left panel of Figure 4), a flatter $z_{\rm in}$ spectrum compared with the $z_{\rm out}$ spectrum is also observed. At the center of HCS, the inward and outward Elsässer variables have the same slope as expected because the two wave populations are not well-separated near the polarity-reversal time.

In Figure 10, we plot the superposed-epoch analysis of the normalized density fluctuation $\delta\rho/\rho$ (blue) and the square of the velocity fluctuation Mach number $(\delta u/C_s)^2$ (orange). During solar minimum, the two quantities are highly correlated, whereas during solar maximum, they are correlated only close to the HCS. We note that our simulation result (Figure 5) also shows high correlation between the two parameters close to the current sheets. However, in the simulation, the density fluctuation is smaller near the HCS compared with the surroundings, in contrast to the observation. The reason is that, in the initial condition of the simulation, we artificially decrease the perturbation amplitude close to the HCS, to avoid discontinuity in the perturbation fields. The increase of the density fluctuation near the HCS from OMNI data might be related to the tearing instability of HCS close to the Sun, which

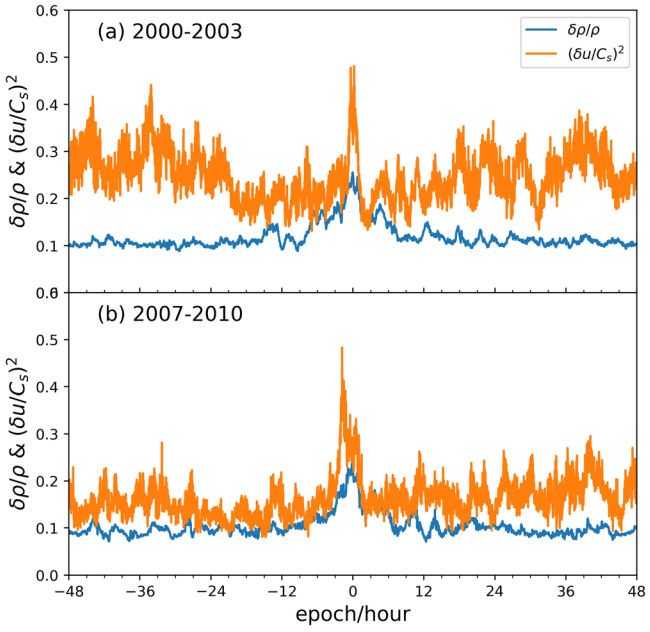

Figure 10. Superposed-epoch analysis of the normalized density fluctuation $\delta\rho/\rho$ (blue) compared with the square of the velocity fluctuation Mach number $(\delta u/C_s)^2$ (orange). Top panel is solar maximum, and bottom panel is solar minimum.

ejects bunches of flux ropes from the tip of helmet streamers (Réville et al. 2020).

4. Discussion

We compare the simulation results from Section 2 and the superposed-epoch analysis from Section 3. In the simulation, σ_c drops in a wide longitudinal range around the current sheet (Figure 2), which is also observed at 1 au (Figure 8). Similarly, in both simulation and observation, σ_r drops in the neighborhood of HCS. Grappin et al. (1991) analyzed four months of Helios 1 data and found that, within the neutral sheet, the turbulence properties are close to the "standard," or fully developed, MHD turbulence, rather than Alfvénic turbulence. Standard MHD turbulence is characterized by balanced outward/inward Elsässer energies and an excess of magnetic energy, consistent with our results. In this scenario, the background magnetic field dissipates the residual energy (the so-called "Alfvén effect"), which is a correlation between the two Elsässer variables generated by intrinsic nonlinear interaction. In other words, the Alfvén effect is essentially the dissipation of two colliding (correlated) counter-propagating Alfvén wave packets as first described by Kraichnan (1965), and hence it is determined by the background magnetic field strength along the wave propagation direction. Thus, the absolute value of the residual energy, regardless of its sign, is larger inside current sheets where the Alfvén effect is weaker. Grappin et al. (1991) explained the balance between outward/inward Elsässer energies at small scales by the fact that the injected energy at large scales due to velocity shear is balanced in $z_{\rm in}$ and $z_{\rm out}$. This interpretation, however, cannot explain the decrease in σ_c around the current sheet in our simulation, because there is no such energy source near the current sheet in the simulation. Instead, the decrease of σ_c around the HCS in the simulation is likely to be a result of the shear of background magnetic field that deforms the wave fronts and facilitates the dissipation of wave energies, similar to the velocity-shear effect. In addition, Grappin et al. (1991) does not answer the question of why the residual energy is negative instead of positive in the current sheets. Here, we propose a mechanism related to the expansion effect of the solar wind. Near the HCS, the weak background magnetic field allows fluctuations to evolve freely so they are dominated by the spherical expansion effect, which leads to $\boldsymbol{u}_\perp$, $\boldsymbol{b}_\perp \sim 1/R$, and $\rho \sim 1/R^2$, and consequently, $\boldsymbol{b}_\perp/\sqrt{\rho} \sim 1$. Hence, as the radial distance increases, the transverse magnetic field fluctuation (in Alfvén speed) becomes larger than the transverse velocity fluctuation, leading to a negative σ_r. This mechanism is supported by Figure 3, which shows that without expansion, no net residual energy is produced. Meanwhile, Figure 3 also shows that the decrease of σ_c cannot be explained by expansion effect and must be caused by processes related to the shear of the background magnetic field.

We note that our simulation cannot explain why, in the solar wind, σ_r is generally negative even far from HCS, as can be seen from Figure 8. Recent studies using Parker Solar Probe data show that σ_r is already negative at below 30 solar radii while σ_c is increasingly high as the satellite moves closer to the Sun (Chen et al. 2020; Shi et al. 2021). Our results show that the presence of a current sheet indeed leads to a dominance of magnetic energy, but it also results in a decrease in σ_c. Thus, the observed ($\sigma_c \approx 0$, $\sigma_r \approx -1$) population of the solar wind fluctuations (e.g., D'Amicis & Bruno 2015) is possibly Alfvénic turbulence evolved under the influence of current sheets, while the prevailing ($\sigma_c \lesssim 1$, $\sigma_r \approx -0.2$) population may be generated in the very young solar wind, with other processes taking effect, or it may be a natural result of the evolution of Alfvénic turbulence (e.g., Boldyrev et al. 2012).

Last, we would like to comment that the statistical study of Alfvénic turbulence properties near SIRs by Borovsky & Denton (2010) shows results quite different from our simulations. Their Figure 11 and Figure 16 show that, at the fast–slow stream interface, the magnetic energy dominance is enhanced, i.e., σ_r decreases, and the Elsässer ratio $|z_{\rm out}|/|z_{\rm in}|$ increases, contradicting our simulation results showing that σ_c declines and σ_r increases at SIRs (Figure 2). The reason for this contradiction is unknown and requires further study.

5. Conclusion

In this study, we carry out two-dimensional MHD simulations, using EBM, and a superposed-epoch analysis, using OMNI data, to study the turbulence properties in the solar wind with a focus on the heliospheric current sheet. The simulation results show that both the normalized cross helicity σ_c and normalized residual energy σ_r drop in the neighborhood of HCS (Figure 2). The observation at 1 au shows that σ_c and σ_r decrease sharply at the center of HCS, on a timescale of 1–2 hr, which is the scale of the HCS crossings (Figure 8). The observation also shows that σ_c starts to drop gradually in a much wider time range $\Delta t > \pm 1$ day, inside the plasma sheet bounding the HCS. The power spectra, calculated over frequency range $f \in [128^{-1}, 2^{-1}]$ minute^{-1} using OMNI data, of velocity, magnetic field, outward and inward Elsässer variables steepen near the HCS (Figure 9), and steeper parallel power spectra near the HCS are also observed in the simulations (Figure 4), implying a stronger energy cascade of the turbulence. Last, both the simulation (Figure 5) and the satellite observation (Figure 10) show that, around the HCS, the density fluctuation $\delta\rho/\rho$ is highly correlated with the square

of the velocity fluctuation Mach number $(\delta u/C_s)^2$, implying a significant compressive component in the velocity fluctuations near the HCS (Grappin et al. 1991).

Our results confirm that current sheets significantly influence the evolution of solar wind turbulence in a way that differs from the velocity shear as discussed by Shi et al. (2020). They may explain the low cross-helicity and magnetic-energy-dominated population of fluctuations in the solar wind, but the origin of the prevailing high cross-helicity and slightly magnetic-energy-dominated fluctuations requires other mechanisms that play important roles close to the Sun, or at the source region of the Alfvénic fluctuations. Inspection of the Parker Solar Probe data is necessary to fully understand these mechanisms.

The OMNI data were obtained from the GSFC/SPDF OMNIWeb interface at https://omniweb.gsfc.nasa.gov. This work used the Extreme Science and Engineering Discovery Environment (XSEDE) EXPANSE at SDSC through allocation No. TG-AST200031, which is supported by National Science Foundation grant number ACI-1548562 (Towns et al. 2014). The work was supported by NASA HERMES DRIVE Science Center grant No. 80NSSC20K0604.

Software: Matplotlib (Hunter 2007).

Appendix
List of Heliospheric Current Sheet Crossings Identified Using OMNI Data

The full list of the HCS crossings is shown in Table 1.

ORCID iDs

Chen Shi (时辰) https://orcid.org/0000-0002-2582-7085
Marco Velli https://orcid.org/0000-0002-2381-3106
Anna Tenerani https://orcid.org/0000-0003-2880-6084
Victor Réville https://orcid.org/0000-0002-2916-3837
Franco Rappazzo https://orcid.org/0000-0001-9030-0418

References

Alazraki, G., & Couturier, P. 1971, A&A, 13, 380
Barkhudarov, M. R. 1991, SoPh, 135, 131
Bavassano, B., Pietropaolo, E., & Bruno, R. 1998, JGR, 103, 6521
Belcher, J. 1971, ApJ, 168, 509
Belcher, J. W., & Davis, Leverett J. 1971, JGR, 76, 3534
Boldyrev, S., Perez, J. C., & Zhdankin, V. 2012, in PHYSICS OF THE HELIOSPHERE: A 10 YEAR RETROSPECTIVE: AIP Conf. Proc. 1436 (Melville, NY: AIP)
Borovsky, J. E., & Denton, M. H. 2010, JGRA, 115, A10
Bruno, R., D'Amicis, R., Bavassano, B., Carbone, V., & Sorriso-Valvo, L. 2007, Ann. Geophys, 25, 1913
Chen, C., Bale, S., Bonnell, J., et al. 2020, ApJS, 246, 53
Chen, C., Chandran, B., Woodham, L., et al. 2021, A&A, 650, L3
Coleman, P. J., J. 1968, ApJ, 153, 371
D'Amicis, R., & Bruno, R. 2015, ApJ, 805, 84
Dobrowolny, M., Mangeney, A., & Veltri, P. 1980, in Solar and Interplanetary Dynamics (Berlin: Springer), 143
Dong, Y., Verdini, A., & Grappin, R. 2014, ApJ, 793, 118
Eselevich, V., & Filippov, M. 1988, P&SS, 36, 105
Goldreich, P., & Sridhar, S. 1995, ApJ, 438, 763
Goldstein, M. L., & Roberts, D. A. 1999, PhPl, 6, 4154
Grappin, R., & Velli, M. 1996, JGR, 101, 425
Grappin, R., Velli, M., & Mangeney, A. 1991, Annales Geophysicae, Vol. 9 (Paris: Gauthier-Villars), 416
Grappin, R., Velli, M., & Mangeney, A. 1993, PhRvL, 70, 2190
Heinemann, M., & Olbert, S. 1980, JGR, 85, 1311
Hellinger, P., Matteini, L., Štverák, Š., Trávníček, P. M., & Marsch, E. 2011, JGRA, 116, A09105
Hollweg, J. V. 1974, JGR, 79, 1539
Hunter, J. D. 2007, CSE, 9, 90
King, J., & Papitashvili, N. 2005, JGRA, 110, A02104
Kiyani, K. H., Osman, K. T., & Chapman, S. C. 2015, RSPTA, 373, 2041
Kraichnan, R. H. 1965, The Physics of Fluids, 8, 1385
Leer, E., Holzer, T. E., & Flå, T. 1982, SSRv, 33, 161
McManus, M. D., Bowen, T. A., Mallet, A., et al. 2020, ApJS, 246, 67
Réville, V., Velli, M., Rouillard, A. P., et al. 2020, ApJL, 895, L20
Roberts, D. A., Goldstein, M. L., Klein, L. W., & Matthaeus, W. H. 1987, JGR, 92, 12023
Roberts, D. A., Goldstein, M. L., Matthaeus, W. H., & Ghosh, S. 1992, JGR, 97, 17115
Shi, C., Velli, M., Tenerani, A., Rappazzo, F., & Réville, V. 2020, ApJ, 888, 68
Shi, C., Velli, M., Panasenco, O., et al. 2021, Astro & Astrophysics, 650, A21
Siscoe, G. 1972, JGR, 77, 27
Smith, E. J. 2001, JGR, 106, 15819
Squire, J., Chandran, B. D., & Meyrand, R. 2020, ApJL, 891, L2
Towns, J., Cockerill, T., Dahan, M., et al. 2014, CSE, 16, 62
Tu, C. Y., Pu, Z. Y., & Wei, F. S. 1984, JGR, 89, 9695
Velli, M. 1993, A&A, 270, 304
Zank, G., Adhikari, L., Hunana, P., et al. 2017, ApJ, 835, 147
Zank, G. P., Matthaeus, W. H., & Smith, C. W. 1996, JGR, 101, 17093
Zhou, Y., & Matthaeus, W. H. 1990, JGR, 95, 14881